BMP9 and BMP10 coordinate liver cellular crosstalk to maintain liver health

Dianyuan Zhao[1,4], Ziwei Huang[1,2,4], Xiaoyu Li[1,2,4], Huan Wang[1,4], Qingwei Hou[1,3], Yuyao Wang[1,3], Fang Yan[1], Wenting Yang[1], Di Liu[1], Shaoqiong Yi[1], Chunguang Han[1], Yanan Hao[1] and Li Tang[1,2,3*]

[1]State Key Laboratory of Medical Proteomics, Beijing Proteome Research Center, National Center for Protein Sciences (Beijing), Beijing Institute of Lifeomics, Beijing, 102206, P.R. China

[2]Department of Immunology, School of Basic Medical Sciences, Anhui Medical University, Hefei, Anhui Province, 230032, P.R. China

[3]School of Basic Medicine, Qingdao University, Qingdao, Shandong Province, 266071, P.R. China

[4]These authors contributed equally

Correspondence:

*(L.T.) E-mail: tangli@ncpsb.org.cn; Tel and Fax: +86-10-61777091

Declaration of interests

The authors declare no competing interests.

Abstract

The liver is the largest solid organ in the body and is primarily composed of HCs, ECs, KCs, and HSCs, which spatially interact and cooperate with each other to maintain liver homeostasis. However, the complexity and molecular mechanisms underlying the crosstalk between these different cell types remain to be revealed. Here, we generated mice with conditional deletion of *Bmp9/10* in different liver cell types and demonstrated that HSCs were the major source of BMP9 and BMP10 in the liver. Using transgenic ALK1 (receptor for BMP9/10) reporter mice, we found that ALK1 is expressed on KCs and ECs other than HCs and HSCs. KCs from *Bmp9/10*$^{\text{HSC-KO}}$ (conditional deletion of *Bmp9/10* from HSCs) mice lost their signature gene expression, such as ID1/3, CLEC4F, VSIG4 and CLEC2, and were replaced by monocyte-derived macrophages. ECs from *Bmp9/10*$^{\text{HSC-KO}}$ mice also lost their identity and were transdifferentiated into continuous ECs, ultimately leading to collagen IV deposition and liver fibrosis. Hepatic ECs express several angiocrine factors, such as BMP2, BMP6, Wnt2 and Rspo3, to regulate liver iron metabolism and metabolic zonation. We found that these angiocrine factors were significantly decreased in ECs from *Bmp9/10*$^{\text{HSC-KO}}$ mice, which further resulted in liver iron overload and disruption of HC zonation. In summary, we demonstrated that HSCs play a central role in mediating liver cell–cell crosstalk via the production of BMP9/10 to maintain liver health.

Introduction

Almost all organs in vertebrates consist of different cell types that undertake their individual functions to maintain organ homeostasis (1), such as vascular endothelial cells supplying oxygen and nutrients to the organ (2) and immune cells, especially tissue-resident macrophages, constantly clearing cell debris and monitoring tissue microenvironments to prevent pathogen infection (3). Usually, these different cell types originate from distinct progenitors and differentiate into specialized cell types via the expression of lineage-specific transcription factors during development (4). Meanwhile, crosstalk between these individual cells within one organ occurs and promotes them to continue to specialize (5, 6), which is needed for the maintenance of the organotypic phenotypes of these cells. However, the cell–cell communication within organs is largely unknown.

The liver is composed of four major cell types: hepatocytes (HCs), Kupffer cells (KCs), endothelial cells (ECs), and hepatic stellate cells (HSCs). The liver exemplifies the importance of cellular interactions in maintaining organ integrity (7-9). For example, secretion of Wnt signaling and BMP2/6 by ECs functions on hepatocytes to control hepatic zonation and iron metabolism (10-13), respectively. Loss of these signals results in liver dysfunction. Recent advances in RNA-sequencing technology and algorithms have enabled a better understanding of the cellular composition and potential cellular interactions of the liver (14). However, the speculative cues still need experimental validation, and more importantly, it is still unknown what consequences happen if specific cell–cell interactions are interrupted.

HSCs reside in the space of Disse and directly interact with HCs, ECs, and KCs (15). HSCs are well known for their pathological role in liver fibrosis, as HSC activation is a critical step in the development of chronic liver disease (16). However, in addition to the storage of retinoids, the physiological role of HSCs in the normal liver remains unclear. ALK1, encoded by the activin A receptor-like type 1 (*Acvrl1*) gene, is the receptor of BMP9 and BMP10. Its mutations result in hereditary hemorrhagic telangiectasia (HHT), which causes vascular malformations in multiple organs, including the liver (17). It has been reported that liver sinusoidal EC-specific *Alk1*-deficient mice exhibit severe liver vascular malformations (18), which mimic the liver symptoms observed in HHT patients. We and others demonstrated that ALK1 is needed

for KC survival and identity, and the ability of KCs from *Alk1*-deficient mice to capture bacteria from the bloodstream was significantly impaired (19, 20). BMP9 is mainly expressed in the liver. Using antibody staining, BMP9 was reported to be expressed in human hepatocytes (21). Recently, based on PCR and scRNA-Seq analysis, BMP9 and BMP10 have been shown to be mainly expressed by murine HSCs (20, 22). However, no study has systematically examined which liver cell types secrete BMP9 and BMP10 and regulate ECs and KCs via these two paracrine factors. Here, we generated mice with conditional knockout of both *Bmp9 and Bmp10* in different liver cell types and found that HSCs are the functional source of BMP9 and BMP10. Interestingly, conditional deletion of *Bmp9/10* from HSCs (*Bmp9/10*$^{\text{HSC-KO}}$) mice not only resulted in loss of KC and EC identity but also affected HC phenotypes in an indirect way, which ultimately resulted in liver dysfunction, suggesting that HSCs play a central role in orchestrating the interactions between different liver cell types under physiological conditions.

Results

HSCs are the functional source of BMP9 and BMP10 in the liver

To generate mice lacking *Bmp9* and *Bmp10* in different liver cell types, *Bmp9*$^{fl/fl}$ and *Bmp10*$^{fl/fl}$ mice were prepared and mated with *Alb*^{Cre}, *Clec4f*^{Cre}, *Tie2*^{Cre}, or *Lrat*^{Cre} mice, which have been extensively used in the literature to produce HCs, KCs, ECs, and HSC conditional knockout mice (12, 19, 23-25), respectively. Because BMP9 and BMP10 play a redundant role in regulating KCs (19), conditional double knockout mice (*Bmp9*$^{fl/fl}$*Bmp10*$^{fl/fl}$*Alb*^{Cre}, *Bmp9*$^{fl/fl}$*Bmp10*$^{fl/fl}$*Tie2*^{Cre}, *Bmp9*$^{fl/fl}$*Bmp10*$^{fl/fl}$*Clec4f*^{Cre} and *Bmp9*$^{fl/fl}$*Bmp10*$^{fl/fl}$*Lrat*^{Cre}) were generated. To systematically investigate which liver cell types produce BMP9 and BMP10, we acquired liver tissues from these mice. Quantitative PCR analysis revealed that *Bmp9* and *Bmp10* mRNA expression was significantly reduced in the liver tissues from *Bmp9*$^{fl/fl}$*Bmp10*$^{fl/fl}$*Lrat*^{Cre} (*Bmp9/10*$^{\text{HSC-KO}}$) mice compared to other Cre deleter mice (Figure 1a). Using Cre-mediated reporter mice, we demonstrated that *Lrat*^{Cre} mice can specifically target HSCs (Figure 1b). BMP10 is mostly expressed in the heart, followed by the liver (26). However, *Bmp10* expression in the heart was not affected in *Bmp9/10*$^{\text{HSC-KO}}$ mice (Figure 1c). ALK1 is the receptor of BMP9/10. To investigate which liver cell types express ALK1 and respond to BMP9/10, we prepared transgenic ALK1 reporter mice, which can faithfully reflect the

expression of ALK1. We found that ALK1 was expressed on ECs and KCs but not HCs and HSCs (Figure 1d), suggesting that BMP9/10 can directly function on ECs and KCs via ALK1. Accordingly, we found that surface markers of liver F4/80^{+} macrophages from *Bmp9/10*$^{\text{HSC-KO}}$ mice, including CLEC4F, Tim4 and VSIG4, were almost not expressed (Figure 1e and 1f). In contrast, these markers were not affected in the liver F4/80^{+} macrophages from *Bmp9*$^{fl/fl}$*Bmp10*$^{fl/fl}$*Alb*^{Cre}, *Bmp9*$^{fl/fl}$*Bmp10*$^{fl/fl}$*Tie2*^{Cre} and *Bmp9*$^{fl/fl}$*Bmp10*$^{fl/fl}$*Clec4f*^{Cre} mice (Supplementary Figure 1). LYVE1 and CLEC2, the surface markers of CD31^{+} hepatic ECs, were also reduced in the livers of *Bmp9/10*$^{\text{HSC-KO}}$ mice (Figure 1g). In addition, we also determined the phenotypes of KCs and ECs from *Bmp10*$^{fl/fl}$*Lrat*^{Cre} mice to exclude the possibility that the altered phenotypes observed in *Bmp9*$^{fl/fl}$*Bmp10*$^{fl/fl}$*Lrat*^{Cre} mice were due to Cre-mediated cytotoxicity (27) and found that these cells were not affected (Supplementary Figure 2). Collectively, these results suggest that HSCs are the functional source of BMP9 and BMP10 in the liver to regulate KCs and ECs.

The differentiation of liver macrophages from *Bmp9/10*$^{\text{HSC-KO}}$ mice is blocked in a status of monocyte-derived macrophages

To acquire more information about transcriptome changes in liver macrophages in the *Bmp9/10*-deficient liver microenvironment, we performed bulk RNA-seq analysis on sorted liver macrophages from *Bmp9/10*$^{\text{HSC-KO}}$ mice compared with their controls. We found that 2424 genes were differentially expressed (FC>2, p-adj<0.05), among which 1313 genes were upregulated and 1111 genes were downregulated in liver macrophages from *Bmp9/10*$^{\text{HSC-KO}}$ mice compared to their control mice (Figure 2a). From these differentially expressed genes, we found that genes associated with the identity of KCs, such as *Fabp7*, *Cd5l*, *Cdh5* and *Clec4f*, were significantly downregulated in liver macrophages from *Bmp9/10*$^{\text{HSC-KO}}$ mice (Figure 2b). *Id1* and *Id3*, target genes of ALK1 signaling and important regulators of KC differentiation, were also significantly reduced in liver macrophages from *Bmp9/10*$^{\text{HSC-KO}}$ mice (Figure 2b). We also observed downregulation of embryonic KC marker *Timd4* (encoding Tim4) expression and upregulation of monocytic *Cx3cr1* and *Ccr2* expression in liver macrophages from *Bmp9/10*$^{\text{HSC-KO}}$ mice (Figure 2c), suggesting that embryonic KCs were lost and replaced by monocyte-derived macrophages/KCs, as a reduced number of liver macrophages was observed in *Bmp9/10*$^{\text{HSC-KO}}$ mice (Figure 2d).

Upon KC loss, blood monocytes are recruited into the liver, immediately differentiate

into F4/80^{+} monocyte-derived macrophages (MoMs) and then gradually acquire the expression of CLEC2, CLEC4F and VSIG4 to become monocyte-derived KCs (MoKCs) with time (15, 28). CLEC2, encoded by *the Clec1b* gene, was thought to be one of the earliest markers gained by monocyte-derived KCs and can be used to discriminate MoKCs from MoMs (29). In addition, TREML4 expression is immediately upregulated upon blood monocyte entry into the liver (25). Interestingly, we found that nearly all liver macrophages from *Bmp9/10*$^{\text{HSC-KO}}$ mice did not express CLEC2 and TREML4, but liver macrophages from *Alk1*$^{fl/fl}$*Vav1*^{Cre} and *Smad4*$^{fl/fl}$*Vav1*^{Cre} mice did (Figure 2e), suggesting that the differentiation of liver macrophages from *Bmp9/10*$^{\text{HSC-KO}}$ mice is completely blocked in a status of monocyte-derived macrophages, and the differentiation defect in liver macrophages from *Bmp9/10*$^{\text{HSC-KO}}$ mice is more pronounced than that from *Alk1*$^{fl/fl}$*Vav1*^{Cre} and *Smad4*$^{fl/fl}$*Vav1*^{Cre} mice. To understand this discrepancy, we performed bulk RNA-seq analysis on sorted liver macrophages from *Smad4*$^{fl/fl}$*Vav1*^{Cre} mice, as Smad4 functions as a common Smad needed for transcriptional regulation in response to ALK signaling. In addition to ALK1, BMP9 and BMP10 also bind ALK2 with low affinity to transduce signals (26). Analysis of the DE genes between *Smad4*-sufficient and *Smad4*-deficient KCs identified 1340 DE genes, including many KC signature genes (Figure 2f and 2g). Comparison of the difference between the DE genes in liver macrophages from *Bmp9/10*$^{\text{HSC-KO}}$ and *Smad4*$^{fl/fl}$*Vav1*^{Cre} mice revealed that 1659 of 2424 DE genes in liver macrophages from *Bmp9/10*$^{\text{HSC-KO}}$ mice did not overlap with DE genes in MoKCs from *Smad4*$^{fl/fl}$*Vav1*^{Cre} mice (Figure 2h), which is consistent with the phenomenon described above, indicating that in addition to Smad4, alterations in other molecular mechanisms may affect the phenotypes of liver macrophages in *Bmp9/10*$^{\text{HSC-KO}}$ mice.

Transcription factors play an important role in the differentiation of tissue-resident macrophages. We compared the nonoverlapping transcription factors between the DE genes in liver macrophages from *Bmp9/10*$^{\text{HSC-KO}}$ and *Smad4*$^{fl/fl}$*Vav1*^{Cre} mice and found 29 transcription factors only downregulated in liver macrophages from *Bmp9/10*$^{\text{HSC-KO}}$ mice (Figure 2i and Supplementary Table 1). Among these transcription factors, we focused on *Rxra* because it has been reported to regulate the development of many embryonic tissue-resident macrophages, including KCs (30), but it is unclear whether RXRa regulates the differentiation of blood monocytes to MoKCs. To test this hypothesis, we prepared *Rxra*$^{fl/fl}$*Csf1r*^{Cre} *Clec4f*^{DTR} mice, in which DT injection can

delete KCs and monocytes recruited into the liver to differentiate into liver macrophages, which can be targeted by the *Csf1r*^{Cre} strain to eliminate the *Rxra* gene (Supplementary Figure 3a). We found that RXRα deficiency significantly inhibited the differentiation of blood monocytes to MoKCs, as the proportion of CLEC2^{+} and VSIG4^{+} macrophages was significantly reduced in *Rxra*-deficient macrophages compared with their controls (Supplementary Figure 3b and 3c), suggesting that the differentiation defect of liver macrophages from *Bmp9/10*$^{\text{HSC-KO}}$ mice may be partially caused by *Rxra* downregulation.

Endothelial cells from *Bmp9/10*$^{\text{HSC-KO}}$ mice are transdifferentiated into continuous endothelial cells

Next, to understand how ECs were affected in *Bmp9/10*$^{\text{HSC-KO}}$ mice, we performed bulk RNA-seq analysis on sorted CD45^{-}CD31^{+} endothelial cells from *Bmp9/10*$^{\text{HSC-KO}}$ mice compared with their controls. We found that 2692 genes were differentially expressed (FC>2, p-adj<0.05), among which 1534 genes were upregulated and 1158 genes were downregulated in ECs from *Bmp9/10*$^{\text{HSC-KO}}$ mice compared to their control mice (Figure 3a). Both GATA4 and MAF act as master regulators of hepatic sinusoidal differentiation (31, 32), and their expression in ECs can be induced by BMP9 *in vitro* (32, 33). In our transcriptomic data, *Gata4* and *Maf* expression in endothelial cells from *Bmp9/10*$^{\text{HSC-KO}}$ mice was significantly reduced compared with that in their controls (Figure 3b). Consistent with the phenotypes of *Gata4/Maf*-deficient endothelial cells, the expression of sinusoidal endothelial cell-specific markers such as *Stab 2*, *Fcgr2b* and *Mrc1* was significantly downregulated (Figure 3c), while the expression of continuous endothelial cell-specific markers such as *Cd34*, *Emcn*, *Apln* and *Aplnr* was upregulated in ECs from *Bmp9/10*$^{\text{HSC-KO}}$ mice (Figure 3d). Immunostaining revealed obviously increased expression of CD34 (Figure 3e). Folw cytometry also confirmed the reduced expression of C-Maf (encoded by *Maf*), CD32b (encoded by *Fcgr2b*), CD117 (encoded by *Kit*) and CD206 (encoded by *Mrc1*) (Figure 3f and 3 g). In addition, genes associated with large arteries were significantly upregulated in ECs from *Bmp9/10*$^{\text{HSC-KO}}$ mice (Figure 3h). These results suggested that hepatic ECs in *Bmp9/10*$^{\text{HSC-KO}}$ mice lost their identity and were transdifferentiated into continuous endothelial and large arterial cells.

Liver metabolic zonation and iron metabolism are disrupted in *Bmp9/10*$^{\text{HSC-KO}}$ mice

Angiocrine factors Wnts and BMP2/6 signal were shown to control hepatic metabolic zonation and iron metabolism (10-13), respectively. The expression of these genes was significantly reduced in ECs from *Bmp9/10*$^{\text{HSC-KO}}$ mice (Figure 4a). Prussian blue staining revealed that 5 out of 7 *Bmp9/10*$^{\text{HSC-KO}}$ mice showed mild iron overload in the focal liver (Figure 4b). Wnt pathway activation induces the expression of zonated proteins such as glutamine synthetase. Immunostaining confirmed the disappearance of glutamine synthetase (GS) in the livers of *Bmp9/10*$^{\text{HSC-KO}}$ mice (Figure 4c), suggesting that liver metabolic zonation was disrupted in *the Bmp9/10*-deficient liver microenvironment.

To acquire more information regarding how the livers were affected under the condition of BMP9/10 deficiency, we performed bulk RNA-seq analysis on whole liver samples of *Bmp9/10*$^{\text{HSC-KO}}$ mice and their control mice at the age of 12 weeks. We analyzed the expression of Wnt signal target genes enriched in the pericentral zone and found that most pericentral Wnt signal targets were significantly downregulated in the livers of *Bmp9/10*$^{\text{HSC-KO}}$ mice, including *Glul*, *Oat*, *Cyp2e1*, *Cyp1a2*, *Cldn2*, *Axin2*, *Lect2*, *Lgr5*, *Tbx3* and *Rnf43* (Figure 4d), supporting the fact that the liver microenvironment in *Bmp9/10*$^{\text{HSC-KO}}$ mice lacks Wnt2, Wnt9b and Rspo3 signaling. In addition, BMP9 and BMP10 play a redundant role in regulating liver metabolic zonation, as glutamine synthetase was still expressed in the livers of *Bmp9*$^{fl/fl}$*Lrat*^{Cre} and *Bmp10*$^{fl/fl}$*Lrat*^{Cre} mice (Figure 4e and 4f).

Liver fibrosis occurs in *Bmp9/10*$^{\text{HSC-KO}}$ mice

Liver weight and the liver/body weight ratio were significantly reduced in *Bmp9/10*$^{\text{HSC-KO}}$ mice at the age of 12W compared with control mice (Figure 5a), suggesting that liver development is impaired. Picrosirius red staining revealed increased collagen deposition in the livers of *Bmp9/10*$^{\text{HSC-KO}}$ mice at the age of 12W (Figure 5b), suggesting that these mice presented liver fibrosis. PDGFB is a profibrotic cytokine that results in HSC activation and liver fibrosis. In the transcriptomic data, we found that *Pdgfb* was significantly upregulated in the liver tissue, ECs and liver macrophages of *Bmp9/10*$^{\text{HSC-KO}}$ mice (Figure 5c). Immunostaining revealed that the expression of desmin and type I collagen, two markers of HSC activation, was upregulated in the liver tissues of *Bmp9/10*$^{\text{HSC-KO}}$ mice (Figure 5d), suggesting that HSC activity was increased. Endothelial Gata4 deficiency leads to sinusoidal capillarization (34). In line with this report, the expression of collagen IV, a marker of EC capillarization, was significantly

increased in the livers of *Bmp9/10*$^{HSC\text{-}KO}$ mice, as revealed by immunostaining (Figure 5e) and the transcriptomic data of ECs (Figure 5f). These results suggested that liver fibrosis in *Bmp9/10*$^{HSC\text{-}KO}$ mice was due to EC capillarization and HSC activation.

Discussion

In this study, we demonstrated that HSCs convey BMP9/10 signals to KCs and ECs to maintain their identity. Loss of BMP9/10 in the liver microenvironment resulted in liver macrophage differentiation defects and a shift in hepatic EC differentiation toward continuous ECs and large arterial cells. Under this condition, physiological crosstalk between ECs and HCs was disrupted, which ultimately altered the whole liver microenvironment and resulted in liver dysfunction.

Recently, we and others have demonstrated that ALK1 is essential for KC differentiation, self-renewal, identity, and endocytic ability (19, 20). Here, we undertook systematic genetic manipulation to scrutinize the functional source of BMP9/10 in the liver. We found that instead of ECs, KCs and HCs, HSCs are the predominant source of BMP9/10 critical for KC homeostasis. BMP9 is mainly expressed in the liver, whereas BMP10 is mostly expressed in the heart and weakly expressed in the liver. We found that BMP10 expression in the heart was not affected in *Bmp9/10*$^{HSC\text{-}KO}$ mice, suggesting that the BMP10 signal needed for KCs and ECs was provided by the local liver rather than circulating BMP10 secreted by the heart. Indeed, ALK1 is weakly expressed in KCs and ECs, as the fluorescence signal emitted by KCs and LSECs from *Alk1*^{tdTomato} reporter mice was weak when detected by flow cytometry, suggesting that the concentration of circulating BMP10 may not be enough to activate ALK1 signaling on hepatic ECs and KCs to maintain their phenotypes.

Recently, Schmid et al. used *Stab 2*^{Cre} mice to delete *Alk1* in liver sinusoidal ECs to model liver HHT (18). They found that upon deletion of *Alk1*, liver sinusoidal ECs lost their identity and were transdifferentiated into large arterial cells. In addition, angiocrine Wnt signaling, such as Wnt2, Wnt9b, and Rspondin3, was impaired in *Alk1*-deficient liver sinusoidal ECs, leading to the disruption of liver metabolic zonation (18). These phenomena were also observed in the *Bmp9/10*$^{HSC\text{-}KO}$ mouse model. However, liver fibrosis observed in HHT patients did not occur in the livers of *Alk1*$^{fl/fl}$*Stab 2*^{Cre} mice (18). Indeed, our transcriptomic data showed that *Stab 2* expression was significantly reduced in hepatic ECs of *Bmp9/10*$^{HSC\text{-}KO\ mice}$, which was consistent with

the data from *Bmp9* KO 129/Ola mice (33), suggesting that ALK1 signaling regulated STAB2 expression. Thus, it is possible that heterozygosity for the *Alk1* deletion in ECs may result in reduced expression of STAB2, and the expression of Cre recombinase driven by the *Stab 2* promoter accordingly decreases, so that the *Alk1*-floxed allele in ECs cannot be efficiently deleted by Cre-mediated cyclization, which may explain why liver fibrosis did not occur in *Alk1*$^{fl/fl}$*Stab 2*^{Cre} mice. In view of liver fibrosis, *Bmp9/10*$^{\text{HSC-KO}}$ mice may be a better mouse model to mimic the liver pathology observed in HHT patients (33). In addition, the liver macrophage niche is composed of HCs, ECs and HSCs (15, 25). Thus, the altered phenotypes of HCs and ECs from *Bmp9/10*$^{\text{HSC-KO}}$ mice may be another reason for the differentiation defect of liver macrophages observed in *Bmp9/10*$^{\text{HSC-KO}}$ mice.

Gata4-deficient mice spontaneously develop liver fibrosis (34). Single-cell RNA-seq analysis of healthy and cirrhotic human liver samples revealed that *Gata4* expression was also reduced in ECs from cirrhotic human liver samples (34), suggesting that reduced expression of *Gata4* may contribute to murine and human liver fibrosis. Given that BMP9/10 regulated the expression of *Gata4* in murine ECs, it is possible that the reduced expression of GATA4 may be due to low expression of BMP9/10 in liver cirrhosis. However, the expression of *Bmp9/10* was not detected by single-cell RNA-seq of either healthy or cirrhotic human livers (35-38) due to the low abundance of *Bmp9/10* mRNA in HSCs. Thus, the correlation between *Bmp9/10* expression and liver fibrosis needs further investigation.

Collectively, we demonstrated that BMP9/10 sourced from HSCs function on KCs and ECs to maintain their identity, which further directs HCs to wire metabolic function to meet the organ's needs. Upon disruption of this crosstalk, liver dysfunction ensued. This work illustrates the complexity underlying the crosstalk between different liver cell types.

Methods

Mice

Bmp9^{fll+} (Stock No: T026617), *Bmp10*$^{fll+}$ (Stock No: T008480), *Tie2*^{Cre} (Stock No: T003764), *Lrat*^{Cre} (Stock No: T006205) and H11 reporter mice (Stock No: T006163) were obtained from GemPharmatech (Nanjing, China). *Alk1*^{tdTomato} mice that an expression cassette encoding tdTomato and a self-cleaving 2A peptide was inserted into the start codon of *Alk1* gene were prepared by MODEL ORGANISMS (Shanghai, China). *Alb*^{Cre} mice (Stock No: 003574) and *Csf1r*^{Cre} (Stock No: 029206) mice were obtained from Jackson Laboratory. *Smad4*$^{fl/fl}$ and *R26*^{YFP} mice were kindly provided by Dr. Xiao Yang (Beijing Institute of Lifeomics). *Alk1*$^{fl/fl}$ mice were kindly provided by Dr. Zhihong Xu (Fudan University, Shanghai). *Vav1*^{Cre} mice were kindly provided by Dr. Bing Liu (Fifth Medical Center of Chinese PLA General Hospital). *Clec4f*$^{Cre/DTR}$ strain mice were established by Nanjing BioMedical Research Institute of Nanjing University (NBRI) using CRISPR/Cas9-mediated genome editing on a C57/BL/6J background. Mice and their littermates were used between eight- to sixteen-week-old unless otherwise specifically indicated. All mice were maintained at the SPF facilities of the Beijing Institute of Lifeomics. All experimental procedures in mice were approved by the Institutional Animal Care and Use Committee at the Beijing Institute of Lifeomics.

Liver cell suspension preparations, flow Cytometry and antibodies

Briefly, the liver was perfused with approximately 20 ml HBSS containing heparin and EDTA, followed by perfusion with digestion buffer containing collagenase type IV (Sigma) and DNase I (Sigma) for 5 min. The digested livers were then disrupted, and pipetted up and down, and the cell suspension was filtered through a 70μm cell strainer. Parenchymal cells were separated from nonparenchymal cells by centrifugation at 50g for 5 min for two times. ECs and liver macrophages were further enriched by iodixanol gradient (OptiPrep) as previously described (39).

Cells were first blocked by anti-CD16/32 antibody and then stained with other appropriate antibodies at 4°C for 20-30 min. 7AAD (559525, BD) was added to dead cell exclusion. Flow cytometry was conducted using an LSRII Fortessa (Becton Dickinson/BD Biosciences). The acquired data were analyzed with FlowJo software (Tree Star). To sort cell, FACSAria III (BD Biosciences) was used. The following

antibodies against mouse proteins were used: anti-CD16/CD32 (2.4G2, TONBO Bioscience), anti-CD45 (30-F11, Biolegend), anti-Ly6C (HK1.4, eBioscience), anti-Ly6G (1A8-Ly6g, eBioscience), anti-CD115 (AFS98, Biolegend), anti-CD64 (x54-5/7.1, BioLegend), anti-F4/80 (BM8, Biolegend), anti-Tim4 (RMT4-54, Biolegend), anti-VSIG4 (NLA14, eBioscience), anti-CD31 (390, Biolegend), anti-CD61 (2C9.G2, Biolegend), anti-CD11b (M1/70, Biolegend), anti-LYVE1 (ALY7 Invitrogen), anti-Treml4 (16E5, Biolegend), anti-CLEC2 (17D9/CLEC-2, Biolegend), anti-CD117 (2B8, Biolegend), anti-CD206 (C068C2, Biolegend), anti-c-Maf (sym0F1, Invitrogen), CD32b (AT130-2, Invitrogen). These antibodies were purchased from eBioscience, Biolegend, TONBO Bioscience, Invitrogen and R&D. Secondary antibody donkey anti-goat IgG was purchased from Invitrogen. The gating strategies for KCs, ECs, HSCs, and HCs were shown in Supplementary figure 4.

Quantitative Real-Time PCR

Total RNA was isolated with Trizol (Thermo) and cDNA was synthesized with Prime Script RT Reagent Kit (Takara). Quantitative PCR was performed with a SYBR Green PCR kit (Toyobo, Japan) in CFX Connect Real-time PCR detection system (Bio-Rad). The specific qPCR primers used are listed in Supplemental Table 2.

RNA-seq analysis

Total RNA of ECs and liver macrophages was isolated with RNeasy plus Mini Kit (Qiagen). Total RNA of the liver tissues was extracted with Trizol (Thermo). Library preparation was performed with UltraTM RNA Library Prep Kit (Illumina) followed by RNA sequencing using NovaSeq 6000 (Illumina). All samples passed quality control based on the results of FastQC. Reads were aligned to the mouse genome assembly mm10.GRCm38 using HISAT2. The aligned reads were counted using FeatureCounts. Differentially expressed genes were determined with DESeq2 program at p-adj (adjusted p value) < 0.05 and logFC (log fold change) > 1 or logFC where indicated. All RNA sequencing experiments were performed with three independent biological replicates. The heatmap and volcano maps of DEGs were visualized using the “ggplot2” and “pheatmap” R package.

Immunohistochemistry and Immunofluorescence

For immunohistochemistry, the livers were fixed in 4% PFA for 12 hours, and then was dehydrated with gradient ethanol and embedded in paraffin. Sections (4μm) were cut on a Finesse 325 (Thermo Scientific) and adhered to adhesion microscope slides. The paraffin sections were dewaxed and hydrated with xylene and gradient ethanol, and then boiled with antigen retrieval solution to repair antigen. Endogenous peroxidase was blocked with 0.3% hydrogen peroxide for 30 minutes. Paraffin sections were blocked with phosphate-buffered saline (PBS) containing 3% horse serum for 1h, and incubated with Avidin and Biotin for 15 minutes, followed by staining with anti-Collagen IV antibody (ab19808, Abcam) overnight at 4℃. Sections were incubated with secondary antibody, ABC reagent and NovaRed peroxidase substrate of Vector-kit (Vector Laboratories) following with the manufacture. Images were acquired on a C10730-12 NanoZoomer with a 20× /NA 0.75 objective lens.

For immunofluorescence, the fixed livers were dehydrated in PBS solutions containing 15% and 30% sucrose for 12 hours, and embedded in OCT compound (Sakura Finetek). The samples were cut into 20-micron slices using the Cryotome FSE (Thermo Scientific) and then attached to Adhesion Microscope slides. Frozen liver sections were then blocked for 2 hours with 1% bovine serum albumin, 0.3 M glycine, and 10% donkey or goat serum before being stained overnight at 4°C with primary antibodies diluted in PBS with 0.2% Tween, secondary antibodies, and Hoechst for 2h at room temperature. Sections were mounted with Fluoromount G (YEASEN) and images were acquired on a Nikon A1R plus N-STORM confocal microscope with a 10x/0.45 PLANAPO, 20X/0.75 PLANAPO or 40X/0.75 PLANFLUOR objective lens. Laser excitation wavelengths of 405 nm, 488 nm, 561 nm, and 647 nm channels were used for sample fluorescence detection. The following antibodies were used, anti-F4/80 (BM8, Biolegend), anti-CD64 (x54-5/7.1, Biolegend), anti-E-Cadherin (147307, Biolegend), anti-CD34 (RAM34, Invitrogen), anti-Glutamine Synthetase (ab49873, Abcam), anti-Desmin (ab15200, Abcam), anti-type I collagen (ab21286, Abcam), and anti-Clec4F (AF2784, R&D systems). Fluorescent-conjugated secondary antibodies were purchased from Jackson ImmunoResearch Laboratories, Abcam and Invitrogen, as

donkey anti rabbit AF594 (711-585-152, Jackson), donkey anti-rat AF488 (ab150153, Abcam), donkey anti-rat AF594 (A21209, Invitrogen) and donkey anti goat FITC (A11055, Invitrogen).

Hematoxylin & eosin (H&E), Picrosirius red (PSR), Nile red and Prussian blue were performed according to standard protocols.

Image processing and analysis

Quantitative analyses of all images were measured using the Fiji package for ImageJ software (NIH) and the Imaris (Oxford Instruments). For coverage measurements of KCs and HSCs, surface modules in Imaris were used to create CD64 and F4/80 biomarkers. A threshold was determined by the algorithm for background subtraction and manually set to match the cell signals. The number of cells per unit area was accessed by parameters in Imaris. IHC and Picrosirius red staining can be assessed by color deconvolution and the thresholding tool in ImageJ.

Statistics

Data are presented as mean ± s.e.m. All statistics analyses were performed in GraphPad Prism (GraphPad Software). Statistical significance was assessed by unpaired, two-tailed, Student's t-test. *$p < 0.05$; **$p < 0.01$; ***$p < 0.001$; ns, not significant. Each symbol represents an individual mouse. Number of animals is indicated as ''n''.

Data availability

The raw RNA-seq data generated from this study have been deposited in NCBI's Gene Expression Omnibus (GEO) under accession number GSE244429.

Author contributions

Z.D., conceived the study, designed and performed the experiments, analyzed flow cytometry data, curated results, wrote the manuscript and made figure panels. H.Z., and L.X., performed the experiments, analyzed the data, and visualized images. W.H., performed bioinformatics analysis and made figure panels. W.Y., L.D., Y.T., Y.S., H.C., and H.Y., provided technical support. T. L., conceived the study, edited the manuscript,

funding acquisition and supervised the study.

Acknowledgements

This work was supported by the National Science Fund for Distinguished Young Scholars of China (82225009) and National Natural Science Foundation of China (32270941). We thank Flow Cytometry Facility, Animal Facility (Mr. Chen Qiu) and Imaging Facility of National Center for Protein Sciences. Beijing (NCPSB) for their assistance.

Reference

1. Regev A, Teichmann SA, Lander ES, Amit I, Benoist C, Birney E, Bodenmiller B, et al. The Human Cell Atlas. Elife 2017;6.
2. Wong BW, Marsch E, Treps L, Baes M, Carmeliet P. Endothelial cell metabolism in health and disease: impact of hypoxia. EMBO J 2017;36:2187-2203.
3. Okabe Y, Medzhitov R. Tissue biology perspective on macrophages. Nat Immunol 2016;17:9-17.
4. Young RA. Control of the embryonic stem cell state. Cell 2011;144:940-954.
5. Pancheva A, Wheadon H, Rogers S, Otto TD. Using topic modeling to detect cellular crosstalk in scRNA-seq. PLoS Comput Biol 2022;18:e1009975.
6. Armingol E, Officer A, Harismendy O, Lewis NE. Deciphering cell-cell interactions and communication from gene expression. Nat Rev Genet 2021;22:71-88.
7. Monga SP. Role and regulation of beta-catenin signaling during physiological liver growth. Gene Expr 2014;16:51-62.
8. Ding C, Li Y, Guo F, Jiang Y, Ying W, Li D, Yang D, et al. A Cell-type-resolved Liver Proteome. Mol Cell Proteomics 2016;15:3190-3202.
9. Azimifar SB, Nagaraj N, Cox J, Mann M. Cell-type-resolved quantitative

proteomics of murine liver. Cell Metab 2014;20:1076-1087.

10. Planas-Paz L, Orsini V, Boulter L, Calabrese D, Pikiolek M, Nigsch F, Xie Y, et al. The RSPO-LGR4/5-ZNRF3/RNF43 module controls liver zonation and size. Nat Cell Biol 2016;18:467-479.

11. Yang J, Mowry LE, Nejak-Bowen KN, Okabe H, Diegel CR, Lang RA, Williams BO, et al. beta-catenin signaling in murine liver zonation and regeneration: a Wnt-Wnt situation! Hepatology 2014;60:964-976.

12. Canali S, Zumbrennen-Bullough KB, Core AB, Wang CY, Nairz M, Bouley R, Swirski FK, et al. Endothelial cells produce bone morphogenetic protein 6 required for iron homeostasis in mice. Blood 2017;129:405-414.

13. Koch PS, Olsavszky V, Ulbrich F, Sticht C, Demory A, Leibing T, Henzler T, et al. Angiocrine Bmp2 signaling in murine liver controls normal iron homeostasis. Blood 2017;129:415-419.

14. Efremova M, Vento-Tormo R, Park JE, Teichmann SA, James KR. Immunology in the Era of Single-Cell Technologies. Annu Rev Immunol 2020;38:727-757.

15. Bonnardel J, T'Jonck W, Gaublomme D, Browaeys R, Scott CL, Martens L, Vanneste B, et al. Stellate Cells, Hepatocytes, and Endothelial Cells Imprint the Kupffer Cell Identity on Monocytes Colonizing the Liver Macrophage Niche. Immunity 2019;51:638-654 e639.

16. Tan Z, Sun H, Xue T, Gan C, Liu H, Xie Y, Yao Y, et al. Liver Fibrosis: Therapeutic Targets and Advances in Drug Therapy. Front Cell Dev Biol 2021;9:730176.

17. Miyazono K, Kamiya Y, Morikawa M. Bone morphogenetic protein receptors and signal transduction. J Biochem 2010;147:35-51.

18. Schmid CD, Olsavszky V, Reinhart M, Weyer V, Trogisch FA, Sticht C, Winkler M, et al. ALK1 controls hepatic vessel formation, angiodiversity, and angiocrine functions in hereditary hemorrhagic telangiectasia of the liver. Hepatology

2023;77:1211-1227.

19. Zhao D, Yang F, Wang Y, Li S, Li Y, Hou F, Yang W, et al. ALK1 signaling is required for the homeostasis of Kupffer cells and prevention of bacterial infection. J Clin Invest 2022;132.

20. Guilliams M, Bonnardel J, Haest B, Vanderborght B, Wagner C, Remmerie A, Bujko A, et al. Spatial proteogenomics reveals distinct and evolutionarily conserved hepatic macrophage niches. Cell 2022;185:379-396 e338.

21. Bidart M, Ricard N, Levet S, Samson M, Mallet C, David L, Subileau M, et al. BMP9 is produced by hepatocytes and circulates mainly in an active mature form complexed to its prodomain. Cell Mol Life Sci 2012;69:313-324.

22. Breitkopf-Heinlein K, Meyer C, Konig C, Gaitantzi H, Addante A, Thomas M, Wiercinska E, et al. BMP-9 interferes with liver regeneration and promotes liver fibrosis. Gut 2017;66:939-954.

23. Lee Y, Leslie J, Yang Y, Ding L. Hepatic stellate and endothelial cells maintain hematopoietic stem cells in the developing liver. J Exp Med 2021;218.

24. Mederacke I, Hsu CC, Troeger JS, Huebener P, Mu X, Dapito DH, Pradere JP, et al. Fate tracing reveals hepatic stellate cells as dominant contributors to liver fibrosis independent of its aetiology. Nat Commun 2013;4:2823.

25. Sakai M, Troutman TD, Seidman JS, Ouyang Z, Spann NJ, Abe Y, Ego KM, et al. Liver-Derived Signals Sequentially Reprogram Myeloid Enhancers to Initiate and Maintain Kupffer Cell Identity. Immunity 2019;51:655-670 e658.

26. Herrera B, Dooley S, Breitkopf-Heinlein K. Potential roles of bone morphogenetic protein (BMP)-9 in human liver diseases. Int J Mol Sci 2014;15:5199-5220.

27. Janbandhu VC, Moik D, Fassler R. Cre recombinase induces DNA damage and tetraploidy in the absence of loxP sites. Cell Cycle 2014;13:462-470.

28. Scott CL, Zheng F, De Baetselier P, Martens L, Saeys Y, De Prijck S, Lippens S, et al. Bone marrow-derived monocytes give rise to self-renewing and fully differentiated Kupffer cells. Nat Commun 2016;7:10321.

29. Tran S, Baba I, Poupel L, Dussaud S, Moreau M, Gelineau A, Marcelin G, et al. Impaired Kupffer Cell Self-Renewal Alters the Liver Response to Lipid Overload during Non-alcoholic Steatohepatitis. Immunity 2020;53:627-640 e625.

30. Philpott J, Kazimierczyk S, Korgaonkar P, Bordt E, Zois J, Vasudevan C, Meng D, et al. RXRalpha Regulates the Development of Resident Tissue Macrophages. Immunohorizons 2022;6:366-372.

31. Geraud C, Koch PS, Zierow J, Klapproth K, Busch K, Olsavszky V, Leibing T, et al. GATA4-dependent organ-specific endothelial differentiation controls liver development and embryonic hematopoiesis. J Clin Invest 2017;127:1099-1114.

32. Gomez-Salinero JM, Izzo F, Lin Y, Houghton S, Itkin T, Geng F, Bram Y, et al. Specification of fetal liver endothelial progenitors to functional zonated adult sinusoids requires c-Maf induction. Cell Stem Cell 2022;29:593-609 e597.

33. Desroches-Castan A, Tillet E, Ricard N, Ouarne M, Mallet C, Belmudes L, Coute Y, et al. Bone Morphogenetic Protein 9 Is a Paracrine Factor Controlling Liver Sinusoidal Endothelial Cell Fenestration and Protecting Against Hepatic Fibrosis. Hepatology 2019;70:1392-1408.

34. Winkler M, Staniczek T, Kurschner SW, Schmid CD, Schonhaber H, Cordero J, Kessler L, et al. Endothelial GATA4 controls liver fibrosis and regeneration by preventing a pathogenic switch in angiocrine signaling. J Hepatol 2021;74:380-393.

35. Ramachandran P, Dobie R, Wilson-Kanamori JR, Dora EF, Henderson BEP, Luu NT, Portman JR, et al. Resolving the fibrotic niche of human liver cirrhosis at single-cell level. Nature 2019;575:512-518.

36. Aizarani N, Saviano A, Sagar, Mailly L, Durand S, Herman JS, Pessaux P, et al. A human liver cell atlas reveals heterogeneity and epithelial progenitors. Nature 2019;572:199-204.

37. MacParland SA, Liu JC, Ma XZ, Innes BT, Bartczak AM, Gage BK, Manuel J, et al. Single cell RNA sequencing of human liver reveals distinct intrahepatic macrophage populations. Nat Commun 2018;9:4383.

38. Lu Y, Yang A, Quan C, Pan Y, Zhang H, Li Y, Gao C, et al. A single-cell atlas of the multicellular ecosystem of primary and metastatic hepatocellular carcinoma. Nat Commun 2022;13:4594.

Methods-only References

39. Ma W, Zhao D, He F, Tang L. The Role of Kupffer Cells as Mediators of Adipose Tissue Lipolysis. J Immunol 2019;203:2689-2700.

Figure legends

Figure 1. HSCs are the major source of BMP9 and BMP10 in the liver.

(a) Quantitative PCR analysis of *Bmp9* and *Bmp10* expression in the liver from the indicated mice. (b) Representative flow cytometric expression of tdTomato in HSCs, HCs, ECs, and KCs from $Lrat^{Cre}H11^{tdTomato}$ mice (n=3/group). (c) Quantitative PCR analysis of *Bmp10* expression in the right atrium from $Bmp9^{fl/fl}Bmp10^{fl/fl}Lrat^{Cre}$ and their littermate controls. (d) Representative flow cytometric expression of tdTomato in HSCs, HCs, ECs, and KCs from $Alk1^{tdTomato}$ mice (n=3/group). (e) Representative immunofluorescence images of liver sections from $Bmp9^{fl/fl}Bmp10^{fl/fl}Lrat^{Cre}$ and their littermate controls at the age of 3-12 weeks (n=6/group). Scale bars: 100μm. (f) Representative flow cytometric expression of Tim4 and VSIG4 in KCs from $Bmp9^{fl/fl}Bmp10^{fl/fl}Lrat^{Cre}$ (n=4) and their littermate controls (n=2). (g) Representative flow cytometric expression of LYVE1 and CLEC2 in ECs from $Bmp9^{fl/fl}Bmp10^{fl/fl}Lrat^{Cre}$ (n=3) and their littermate controls (n=3). Results represent the mean ± SEM. *P < 0.05, **P < 0.01, ***P < 0.001, and ****P <0.0001, by 2-tailed Student's t test (a,c).

Figure 2. The differentiation of liver macrophages was inhibited in $Bmp9^{fl/fl}Bmp10^{fl/fl}Lrat^{Cre}$ mice.

(a) Volcano plot of the RNA-seq data of sorted liver macrophages from $Bmp9^{fl/fl}Bmp10^{fl/fl}Lrat^{Cre}$ and control mice. Genes upregulated and downregulated are shown in red and blue, respectively (fold change [FC] > 2, adjusted p[p-adj] < 0.05). (b) Heatmap showing signature genes expressed differentially in liver macrophages from $Bmp9^{fl/fl}Bmp10^{fl/fl}Lrat^{Cre}$ and control mice. (c) Expression counts of indicated genes in liver macrophages from $Bmp9^{fl/fl}Bmp10^{fl/fl}Lrat^{Cre}$ and control mice. (d) Immunofluorescence images of $F4/80^{+}$ and $CD64^{+}$ liver macrophages in sections from $Bmp9^{fl/fl}Bmp10^{fl/fl}Lrat^{Cre}$ mice and their controls. Liver macrophages number was measured (right). (e) Flow cytometric expression of CLEC2 and TREML4 in liver macrophages from the indicated mice (n=3-4/group). (f) Volcano plot of the RNA-seq data of sorted liver macrophages from $Smad4^{fl/fl}Vav1^{Cre}$ and control mice. Genes

upregulated and downregulated are shown in red and blue, respectively (fold change [FC] > 2, adjusted p[p-adj] < 0.05). (g) Heatmap showing signature genes expressed differentially in liver macrophages from *Smad4*$^{fl/fl}$*Vav1*^{Cre} and control mice. (h, i) Venn diagram showing DE genes (h) and transcription factors (i) specific to liver macrophages of *Bmp9*$^{fl/fl}$*Bmp10*$^{fl/fl}$*Lrat*^{Cre}, *Smad4*-deficient liver macrophages or shared between both mac populations. Results represent the mean ± SEM. *P < 0.05, **P <0.01, ***P < 0.001, and ****P <0.0001, by 2-tailed Student's t test (c, d).

Figure 3. Endothelial cells from *Bmp9*$^{fl/fl}$*Bmp10*$^{fl/fl}$*Lrat*^{Cre} mice are transdifferentiated to continuous endothelial cells.

(a) Volcano plot of the RNA-seq data of sorted hepatic ECs from *Bmp9*$^{fl/fl}$*Bmp10*$^{fl/fl}$*Lrat*^{Cre} and control mice. Genes upregulated and downregulated are shown in red and blue, respectively (fold change [FC] > 2, adjusted p[p-adj] < 0.05). (b) Expression counts of Gata4 and Maf genes in ECs from *Bmp9*$^{fl/fl}$*Bmp10*$^{fl/fl}$*Lrat*^{Cre} and control mice. (c, d) Heatmap showing sinusoidal EC-associated genes (c) and continuous EC-associated genes (d) expressed differentially in hepatic ECs from *Bmp9*$^{fl/fl}$*Bmp10*$^{fl/fl}$*Lrat*^{Cre} and control mice. (e) Representative immunofluorescence images in liver sections from *Bmp9*$^{fl/fl}$*Bmp10*$^{fl/fl}$*Lrat*^{Cre} and control mice (n=4/group). Scale bars: 100μm. (f, g) Flow cytometric expression of CD32b, C-Maf, CD206 and CD117 in hepatic ECs from *Bmp9*$^{fl/fl}$*Bmp10*$^{fl/fl}$*Lrat*^{Cre} and littermate controls (n=4-5/group). (h) Heatmap showing the indicated genes expressed differentially in hepatic ECs from *Bmp9*$^{fl/fl}$*Bmp10*$^{fl/fl}$*Lrat*^{Cre} and control mice. Results represent the mean ± SEM. *P < 0.05, **P < 0.01, ***P < 0.001, and ****P <0.0001, by 2-tailed Student's t test (b).

Figure 4. Liver metabolic zonation and iron metabolism are disrupted in *Bmp9*$^{fl/fl}$*Bmp10*$^{fl/fl}$*Lrat*^{Cre} mice.

(a) Heatmap showing the indicated genes expressed differentially in hepatic ECs from *Bmp9*$^{fl/fl}$*Bmp10*$^{fl/fl}$*Lrat*^{Cre} and control mice. (b) Prussian blue in livers from *Bmp9*$^{fl/fl}$*Bmp10*$^{fl/fl}$*Lrat*^{Cre} mice and their controls. (c) Representative immunofluorescence images in liver sections from *Bmp9*$^{fl/fl}$*Bmp10*$^{fl/fl}$*Lrat*^{Cre} mice and their controls (n=5/group). Scale bars: 200μm. (d) Heatmap showing the indicated

genes expressed differentially in liver tissues from *Bmp9*$^{fl/fl}$*Bmp10*$^{fl/fl}$*Lrat*^{Cre} and control mice at the age of 12W. (e, f) Representative immunofluorescence images in liver sections from *Bmp9*$^{fl/fl}$*Lrat*^{Cre} (e) and *Bmp10*$^{fl/fl}$*Lrat*^{Cre} (f) mice and their controls (n=2/group). Scale bars: 200μm.

Figure 5. Liver fibrosis occurs in *Bmp9*$^{fl/fl}$*Bmp10*$^{fl/fl}$*Lrat*^{Cre} mice.

(a) Liver weight and liver to body weight ratio of *Bmp9*$^{fl/fl}$*Bmp10*$^{fl/fl}$*Lrat*^{Cre} mice and their littermate controls at the age of 12W. (b) PSR staining of liver sections from *Bmp9*$^{fl/fl}$*Bmp10*$^{fl/fl}$*Lrat*^{Cre} mice and their controls. Scale bars: 100μm. (c) Expression counts of *Pdgfb* gene in liver tissues (left), endothelial cells (middle) and liver macrophages (right) from *Bmp9*$^{fl/fl}$*Bmp10*$^{fl/fl}$*Lrat*^{Cre} mice and their control mice. (d) Immunofluorescence images of Desmin and collagen I in liver sections in liver tissues from *Bmp9*$^{fl/fl}$*Bmp10*$^{fl/fl}$*Lrat*^{Cre} (12-28W) and control mice. (e) Collagen IV immunohistochemistry staining of liver sections from *Bmp9*$^{fl/fl}$*Bmp10*$^{fl/fl}$*Lrat*^{Cre} mice and their controls. Scale bars:100μm. (f) Expression counts of indicated genes in endothelial cells from *Bmp9*$^{fl/fl}$*Bmp10*$^{fl/fl}$*Lrat*^{Cre} and control mice. Results represent the mean± SEM. *P < 0.05, **P < 0.01, ***P < 0.001, and ****P <0.0001, by 2-tailed Student's t test (a-f).

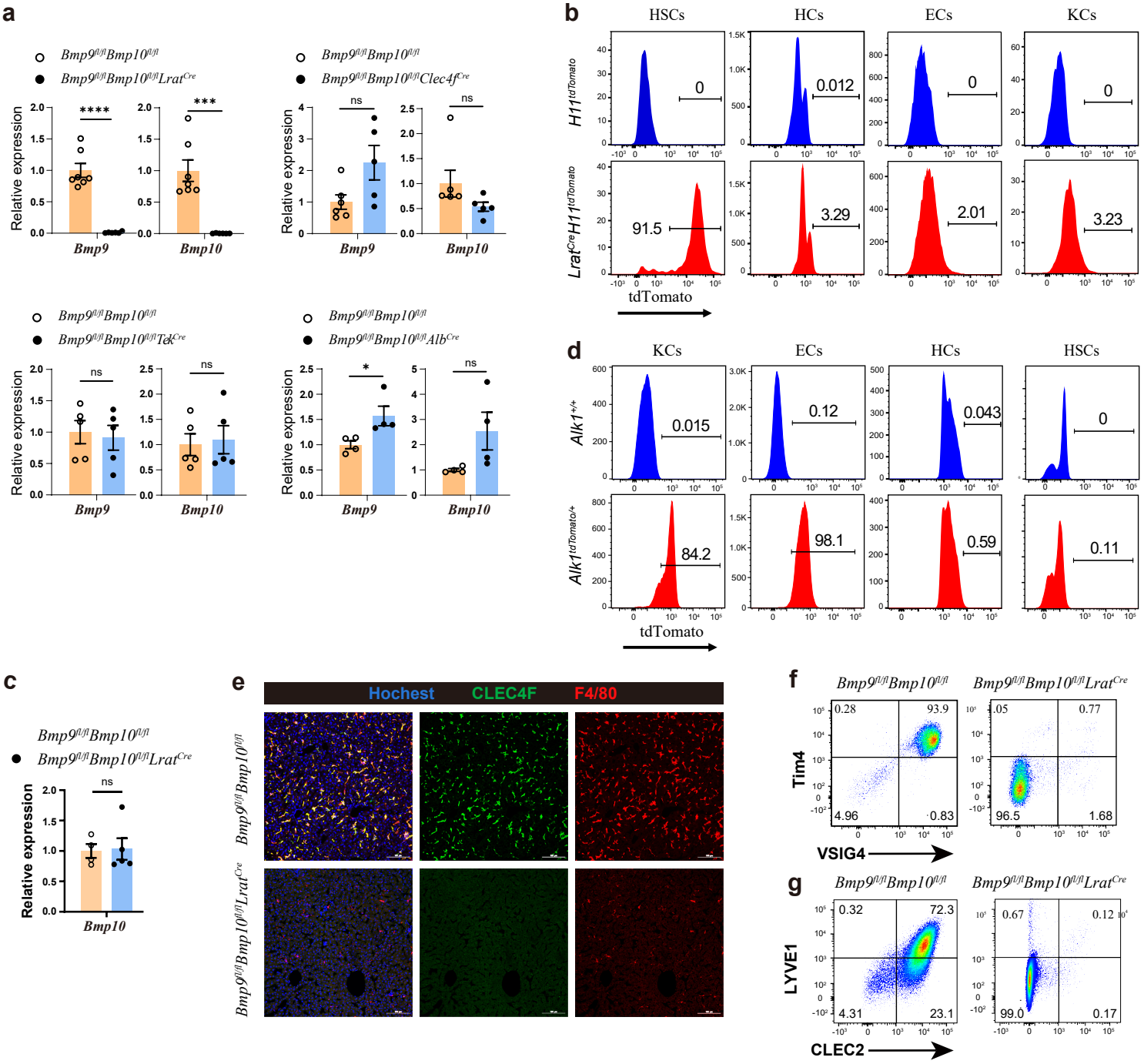

Figure 1. HSCs are the major source of BMP9 and BMP10 in the liver.

(a) Quantitative PCR analysis of *Bmp9* and *Bmp10* expression in the liver from the indicated mice.

(b) Representative flow cytometric expression of tdTomato in HSCs, HCs, ECs, and KCs from $Lrat^{Cre}H11^{tdTomato}$ mice (n=3/group).

(c) Quantitative PCR analysis of *Bmp10* expression in the right atrium from $Bmp9^{fl/fl}Bmp10^{fl/fl}Lrat^{Cre}$ and their littermate controls.

(d) Representative flow cytometric expression of tdTomato in HSCs, HCs, ECs, and KCs from $Alk1^{tdTomato}$ mice (n=3/group).

(e) Representative immunofluorescence images of liver sections from $Bmp9^{fl/fl}Bmp10^{fl/fl}Lrat^{Cre}$ and their littermate controls at the age of 3-12 weeks (n=6/group). Scale bars: 100μm.

(f) Representative flow cytometric expression of Tim4 and VSIG4 in KCs from $Bmp9^{fl/fl}Bmp10^{fl/fl}Lrat^{Cre}$ (n=4) and their littermate controls (n=2).

(g) Representative flow cytometric expression of LYVE1 and CLEC2 in ECs from $Bmp9^{fl/fl}Bmp10^{fl/fl}Lrat^{Cre}$ (n=3) and their littermate controls (n=3). Results represent the mean ± SEM. *P < 0.05, **P < 0.01, ***P < 0.001, and ****P <0.0001, by 2-tailed Student's t test (a,c).

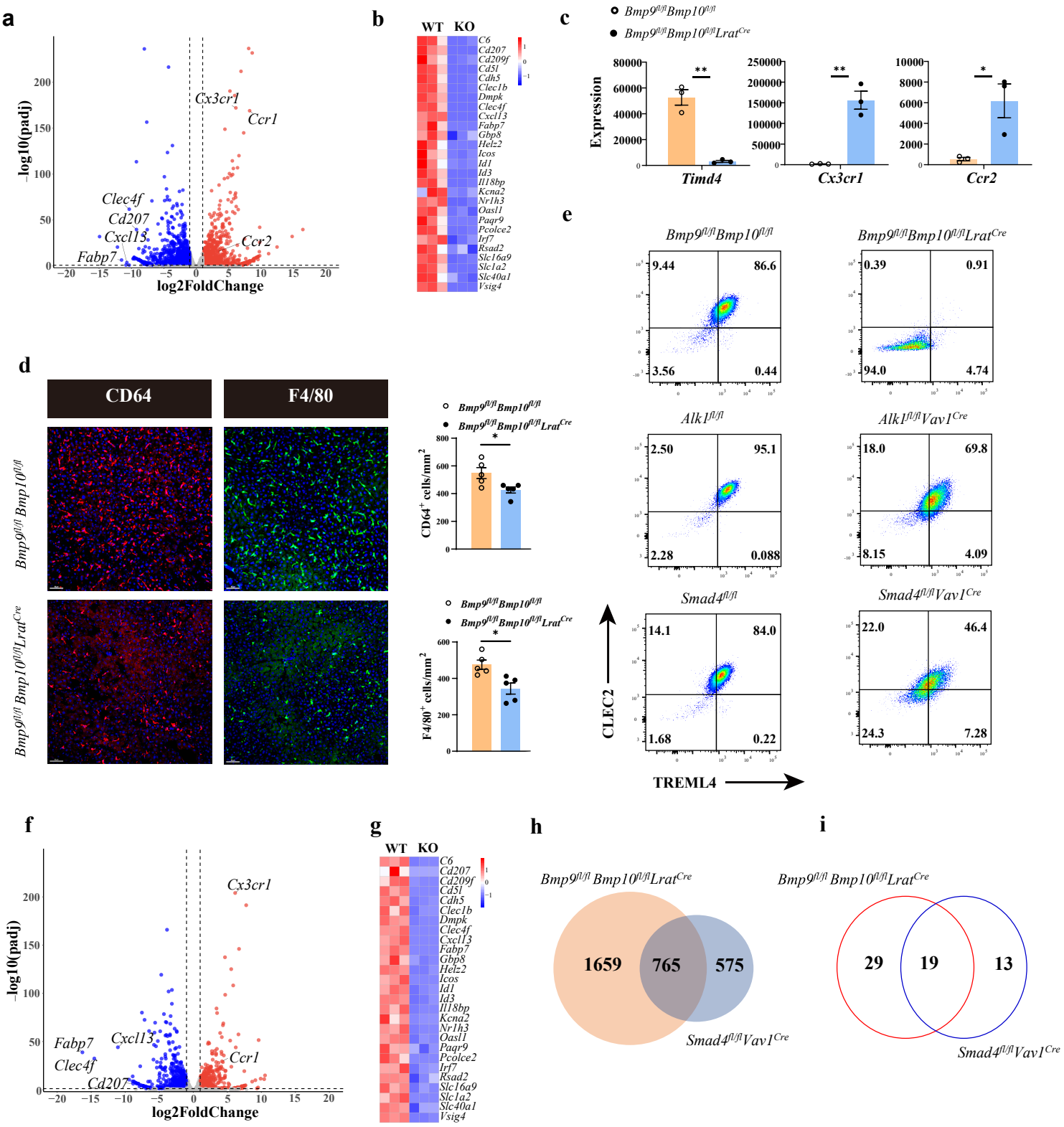

Figure 2. The differentiation of liver macrophages was inhibited in *Bmp9$^{fl/fl}$Bmp10$^{fl/fl}$Lrat^{Cre}* mice.

(a) Volcano plot of the RNA-seq data of sorted liver macrophages from *Bmp9$^{fl/fl}$Bmp10$^{fl/fl}$Lrat^{Cre}* and control mice. Genes upregulated and downregulated are shown in red and blue, respectively (fold change [FC] > 2, adjusted p[p-adj] < 0.05).
(b) Heatmap showing signature genes expressed differentially in liver macrophages from *Bmp9$^{fl/fl}$Bmp10$^{fl/fl}$Lrat^{Cre}* and control mice.
(c) Expression counts of indicated genes in liver macrophages from *Bmp9$^{fl/fl}$Bmp10$^{fl/fl}$Lrat^{Cre}* and control mice.
(d) Immunofluorescence images of F4/80^{+} and CD64^{+} liver macrophages in sections from *Bmp9$^{fl/fl}$Bmp10$^{fl/fl}$Lrat^{Cre}* mice and their controls. Liver macrophages number was measured (right).
(e) Flow cytometric expression of CLEC2 and TREML4 in liver macrophages from the indicated mice (n=3-4/group).
(f) Volcano plot of the RNA-seq data of sorted liver macrophages from *Smad4$^{fl/fl}$Vav1^{Cre}* and control mice. Genes upregulated and downregulated are shown in red and blue, respectively (fold change [FC] > 2, adjusted p[p-adj] < 0.05).
(g) Heatmap showing signature genes expressed differentially in liver macrophages from *Smad4$^{fl/fl}$Vav1^{Cre}* and control mice.
(h, i) Venn diagram showing DE genes (h) and transcription factors (i) specific to liver macrophages of *Bmp9$^{fl/fl}$Bmp10$^{fl/fl}$Lrat^{Cre}*, *Smad4*-deficient liver macrophages or shared between both mac populations. Results represent the mean ± SEM. *P < 0.05, **P < 0.01, ***P < 0.001, and ****P <0.0001, by 2-tailed Student's t test (c, d).

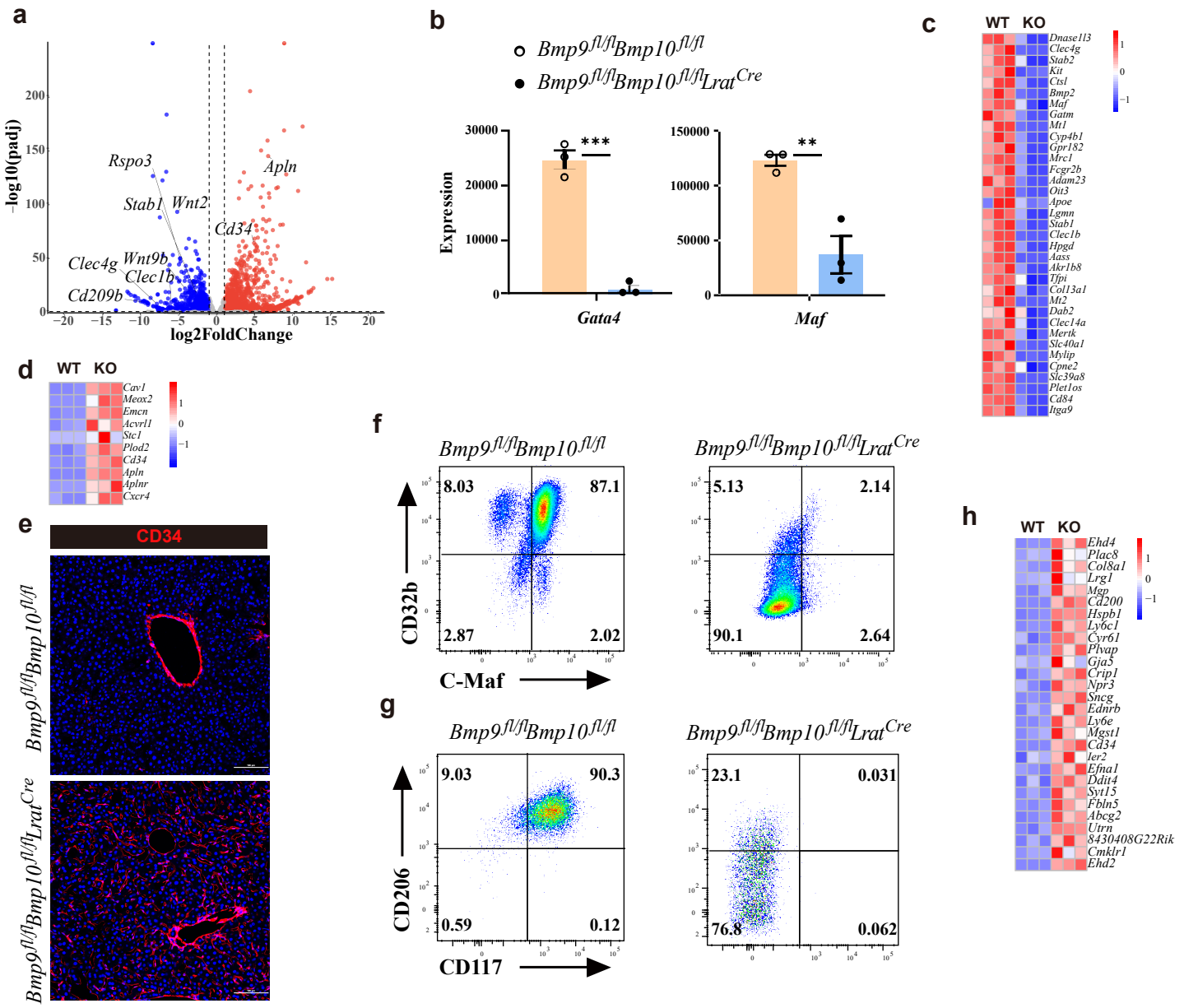

Figure 3. Endothelial cells from *Bmp9*$^{fl/fl}$*Bmp10*$^{fl/fl}$*Lrat*^{Cre} mice are transdifferentiated to continuous endothelial cells.

(a) Volcano plot of the RNA-seq data of sorted hepatic ECs from *Bmp9*$^{fl/fl}$*Bmp10*$^{fl/fl}$*Lrat*^{Cre} and control mice. Genes upregulated and downregulated are shown in red and blue, respectively (fold change [FC] > 2, adjusted p[p-adj] < 0.05).

(b) Expression counts of Gata4 and Maf genes in ECs from *Bmp9*$^{fl/fl}$*Bmp10*$^{fl/fl}$*Lrat*^{Cre} and control mice.

(c, d) Heatmap showing sinusoidal EC-associated genes (c) and continuous EC-associated genes (d) expressed differentially in hepatic ECs from *Bmp9*$^{fl/fl}$*Bmp10*$^{fl/fl}$*Lrat*^{Cre} and control mice.

(e) Representative immunofluorescence images in liver sections from *Bmp9*$^{fl/fl}$*Bmp10*$^{fl/fl}$*Lrat*^{Cre} and control mice (n=4/group).Scale bars: 100μm.

(f, g) Flow cytometric expression of CD32b, C-Maf, CD206 and CD117 in hepatic ECs from *Bmp9*$^{fl/fl}$*Bmp10*$^{fl/fl}$*Lrat*^{Cre} and littermate controls (n=4-5/group).

(h) Heatmap showing the indicated genes expressed differentially in hepatic ECs from *Bmp9*$^{fl/fl}$*Bmp10*$^{fl/fl}$*Lrat*^{Cre} and control mice. Results represent the mean ± SEM. *P < 0.05, **P < 0.01, ***P < 0.001, and ****P <0.0001, by 2-tailed Student's t test (b).

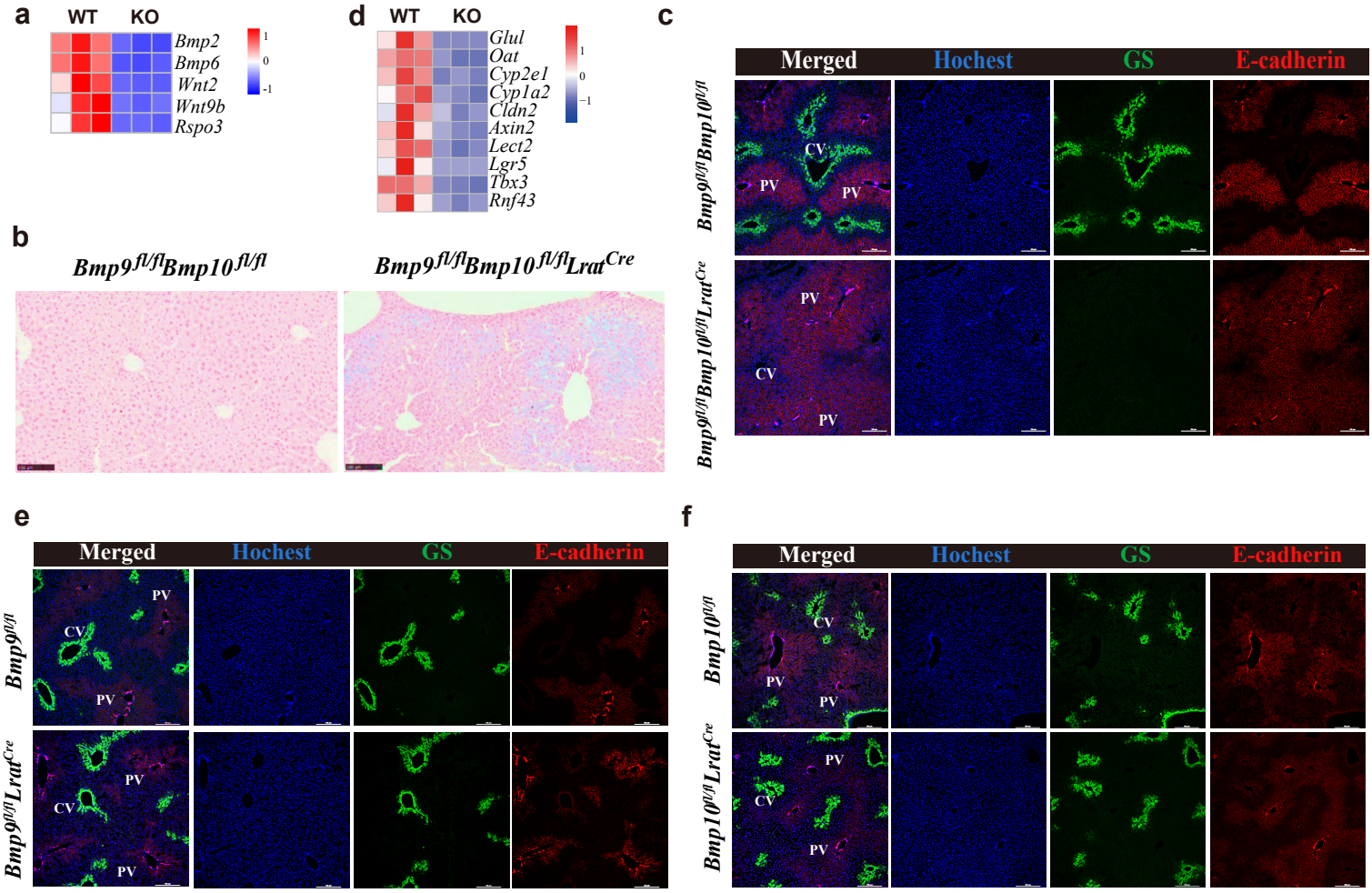

Figure 4. Liver metabolic zonation and iron metabolism are disrupted in *Bmp9$^{fl/fl}$Bmp10$^{fl/fl}$Lrat^{Cre}* mice.

(a) Heatmap showing the indicated genes expressed differentially in hepatic ECs from *Bmp9$^{fl/fl}$Bmp10$^{fl/fl}$Lrat^{Cre}* and control mice.

(b) Prussian blue in livers from *Bmp9$^{fl/fl}$Bmp10$^{fl/fl}$Lrat^{Cre}* mice and their controls.

(c) Representative immunofluorescence images in liver sections from *Bmp9$^{fl/fl}$Bmp10$^{fl/fl}$Lrat^{Cre}* mice and their controls (n=5/group). Scale bars: 200μm.

(d) Heatmap showing the indicated genes expressed differentially in liver tissues from *Bmp9$^{fl/fl}$Bmp10$^{fl/fl}$Lrat^{Cre}* and control mice at the age of 12W.

(e, f) Representative immunofluorescence images in liver sections from *Bmp9$^{fl/fl}$Lrat^{Cre}* (e) and *Bmp10$^{fl/fl}$Lrat^{Cre}* (f) mice and their controls (n=2/group). Scale bars: 200μm.

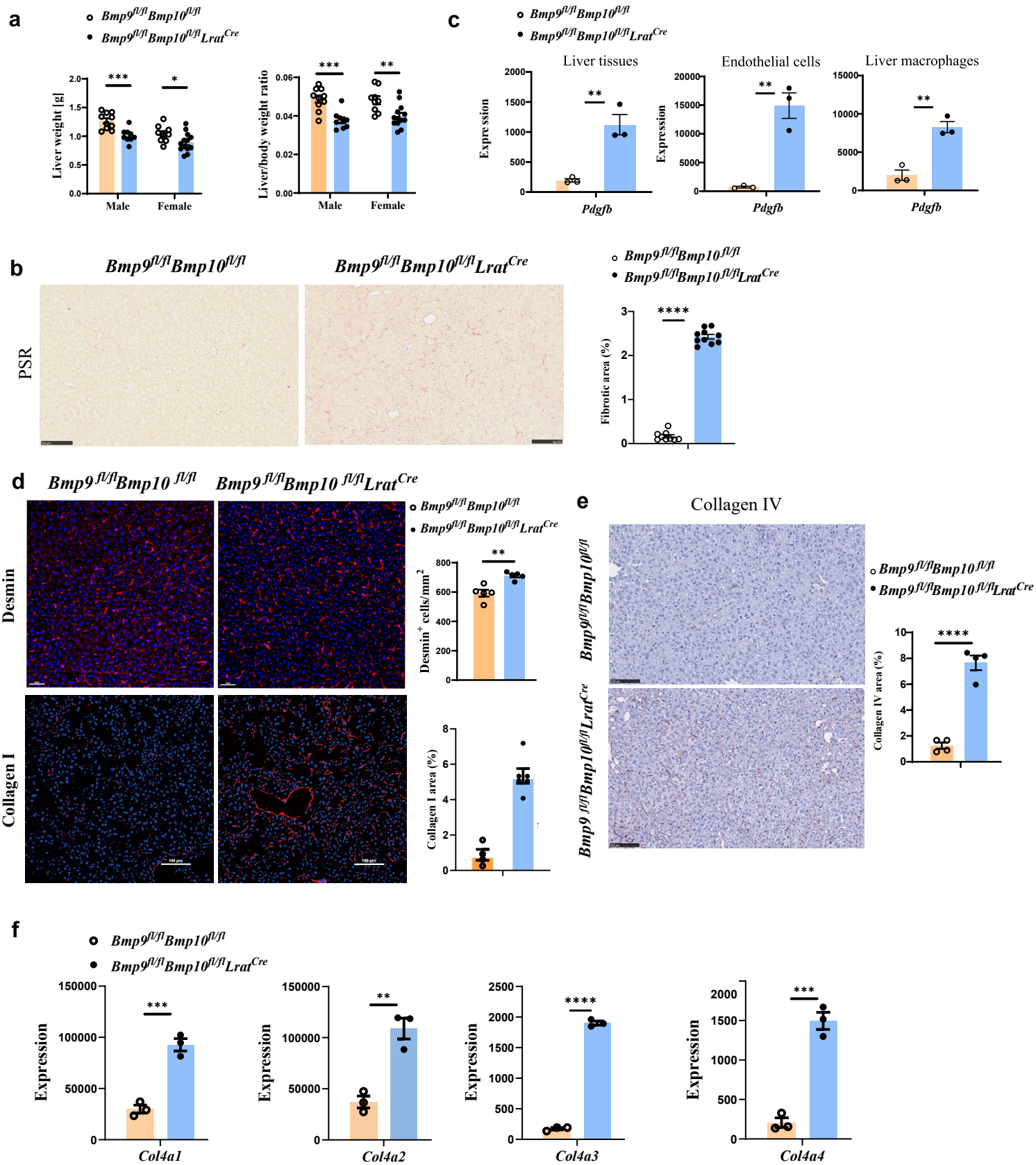

Figure 5. Liver fibrosis occurs in *Bmp9*$^{fl/fl}$*Bmp10*$^{fl/fl}$*Lrat*^{Cre} mice.

(a) Liver weight and liver to body weight ratio of *Bmp9*$^{fl/fl}$*Bmp10*$^{fl/fl}$*Lrat*^{Cre} mice and their littermate controls at the age of 12W.
(b) PSR staining of liver sections from *Bmp9*$^{fl/fl}$*Bmp10*$^{fl/fl}$*Lrat*^{Cre} mice and their controls. Scale bars: 100μm.
(c) Expression counts of *Pdgfb* gene in liver tissues (left), endothelial cells (middle) and liver macrophages (right) from *Bmp9*$^{fl/fl}$*Bmp10*$^{fl/fl}$*Lrat*^{Cre} mice and their control mice.
(d) Immunofluorescence images of Desmin and collagen I in liver sections in liver tissues from *Bmp9*$^{fl/fl}$*Bmp10*$^{fl/fl}$*Lrat*^{Cre} (12-28W) and control mice.
(e) Collagen IV immunohistochemistry staining of liver sections from *Bmp9*$^{fl/fl}$*Bmp10*$^{fl/fl}$*Lrat*^{Cre} mice and their controls. Scale bars: 100μm.
(f) Expression counts of indicated genes in endothelial cells from *Bmp9*$^{fl/fl}$*Bmp10*$^{fl/fl}$*Lrat*^{Cre} and control mice. Results represent the mean ± SEM. *P < 0.05, **P < 0.01, ***P < 0.001, and ****P <0.0001, by 2-tailed Student's t test (a-f).

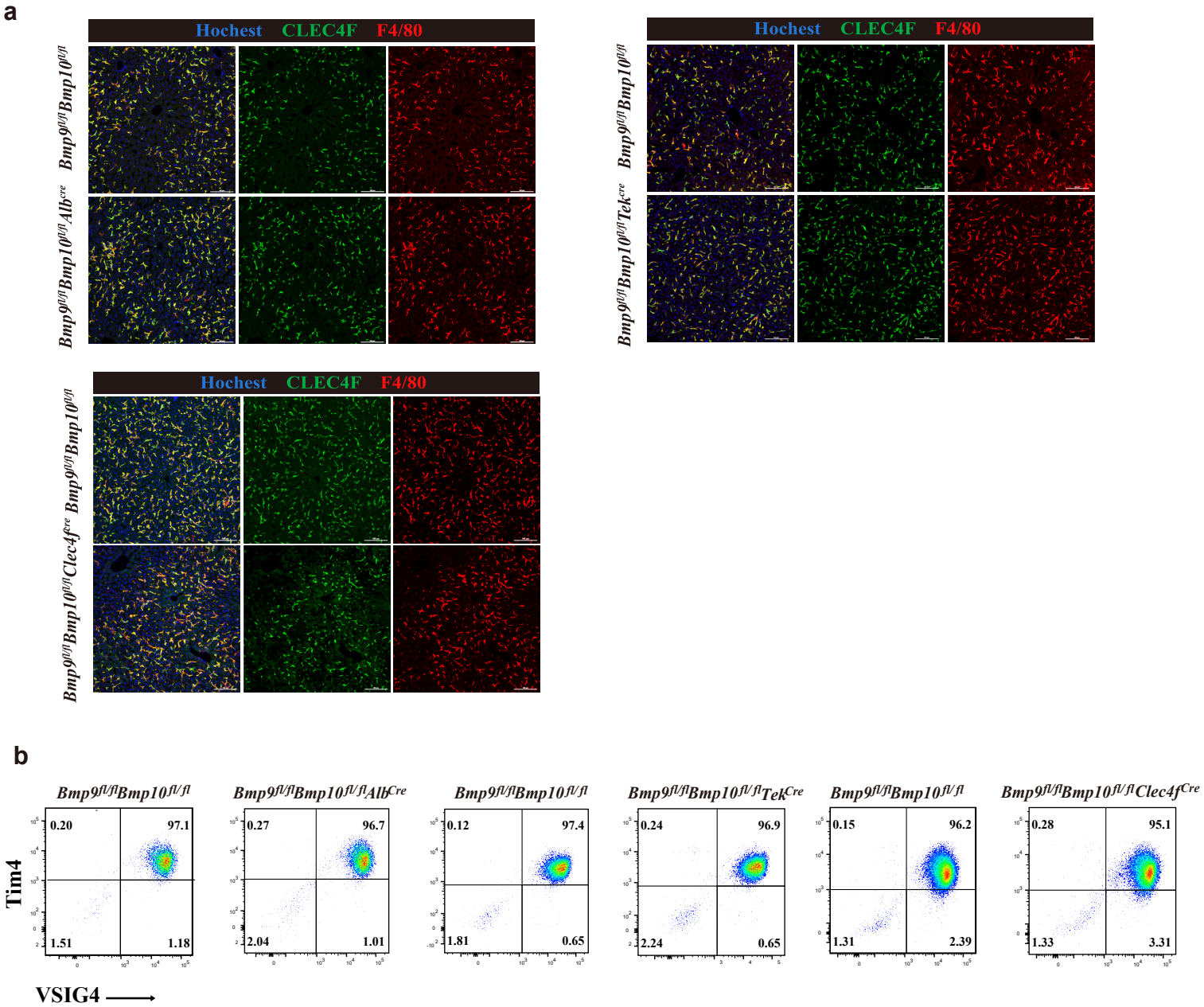

Supplementary Figure 1. The phenotypes of KCs were not affected in the liver from *Bmp9*$^{fl/fl}$*Bmp10*$^{fl/fl}$*Alb*^{Cre}, *Bmp9*$^{fl/fl}$*Bmp10*$^{fl/fl}$*Tek*^{Cre} and *Bmp9*$^{fl/fl}$*Bmp10*$^{fl/fl}$*Clec4f*^{Cre} mice.

(a) Representative immunofluorescence images of liver sections from the indicated mice (n=3-5/group). Scale bars: 100μm.

(b) Representative flow cytometric expression of Tim4 and VSIG4 in KCs from the indicated mice (n=3-5/group).

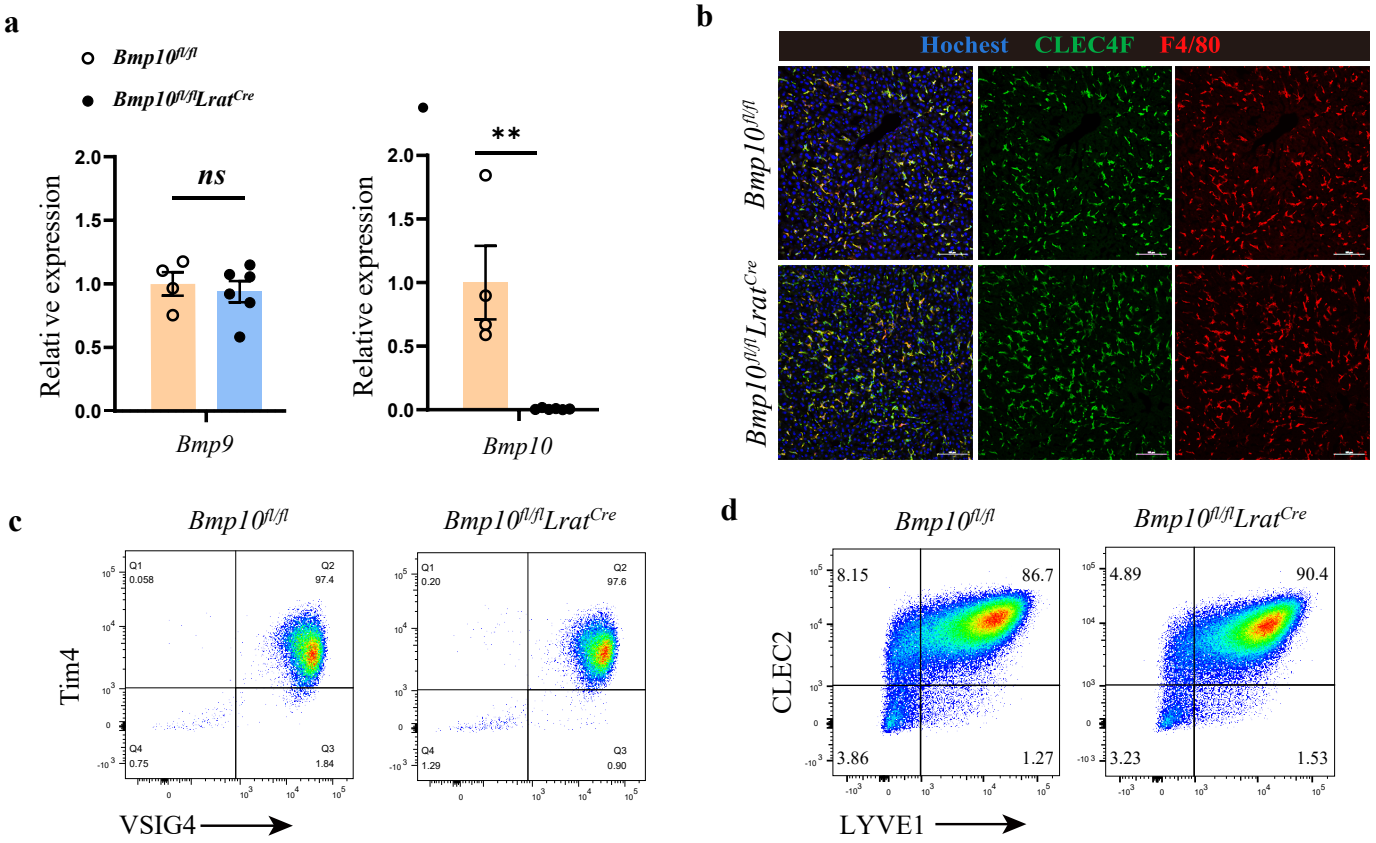

Supplementary Figure 2. BMP10 can compensate the role of BMP9 in the liver.
(a) Quantitative PCR analysis of *Bmp9* and *Bmp10* expression in the liver from *Bmp10*$^{fl/fl}$*Lrat*^{Cre} and their littermate controls.
(b) Representative immunofluorescence images of liver sections from the indicated mice (n=4/group). Scale bars: 100μm.
(c-d) Representative flow cytometric expression of the indicated markers in KCs (c) and ECs (d) from *Bmp10*$^{fl/fl}$*Lrat*^{Cre} and their littermate controls (n=2/group). Results represent the mean ± SEM. *P < 0.05, **P < 0.01, 0.0001, by 2-tailed Student's t test (a).

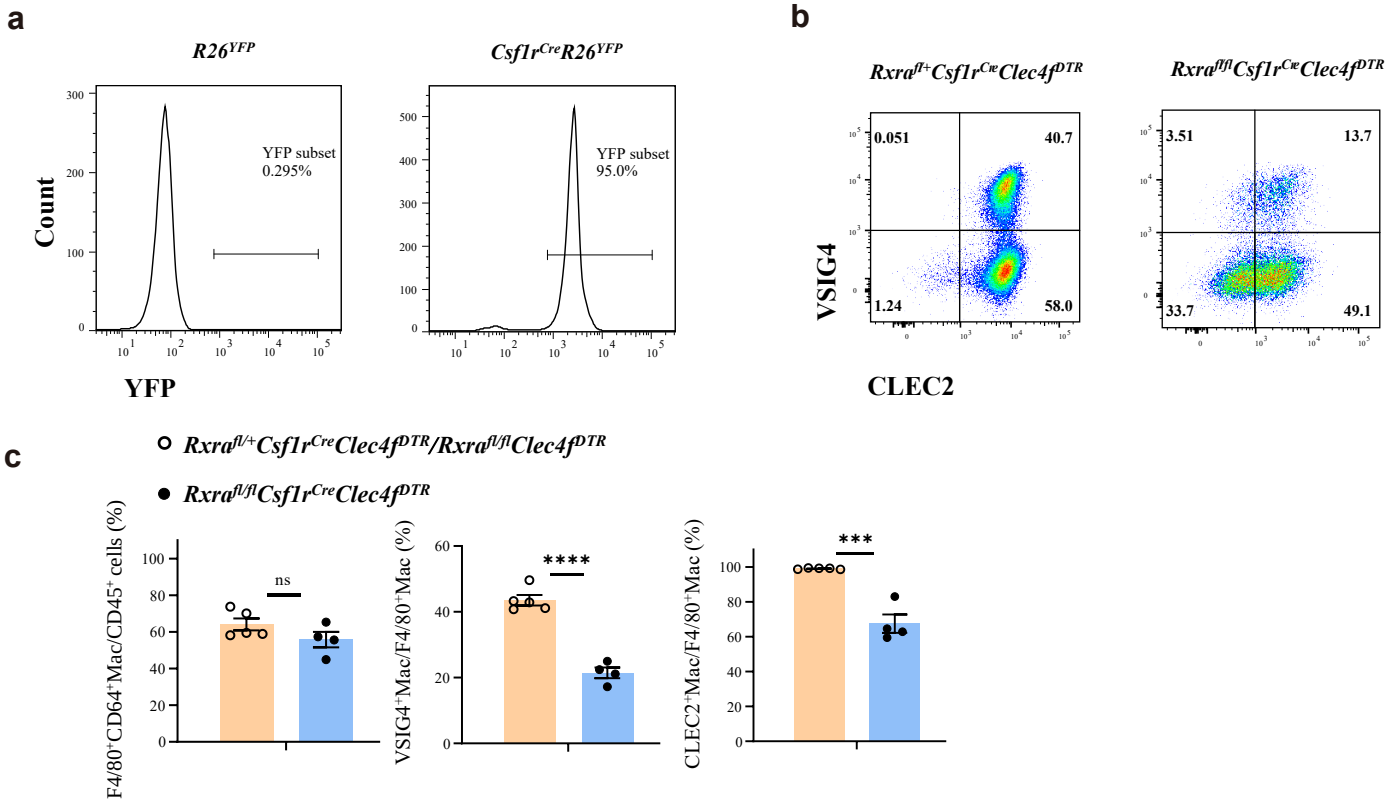

Supplementary Figure 3. RXRα is required for the differentiation from blood monocytes to MoKCs.
(a) Representative flow cytometric expression of YFP in blood monocytes from *Csf1r*^{Cre}*R26*^{YFP} and control mice (n=2/group).
(b,c) Representative flow cytometric expression (b) of CLEC2 and VSIG4 in liver macrophages, and percentage (c) of F4/80^{+}, VSIG4^{+} and CLEC2^{+} liver macrophages from *Rxra*$^{fl/fl}$*Csf1r*^{Cre}*Clec4f*^{DTR} mice and controls. The indicated mice were injected with 200ng/mice diphtheria toxin via IP. After 7 days, VSIG4 and CLEC2 expression in liver macrophages were assessed. Results represent the mean ± SEM. *P < 0.05, **P < 0.01, 0.0001, by 2-tailed Student's t test (B).

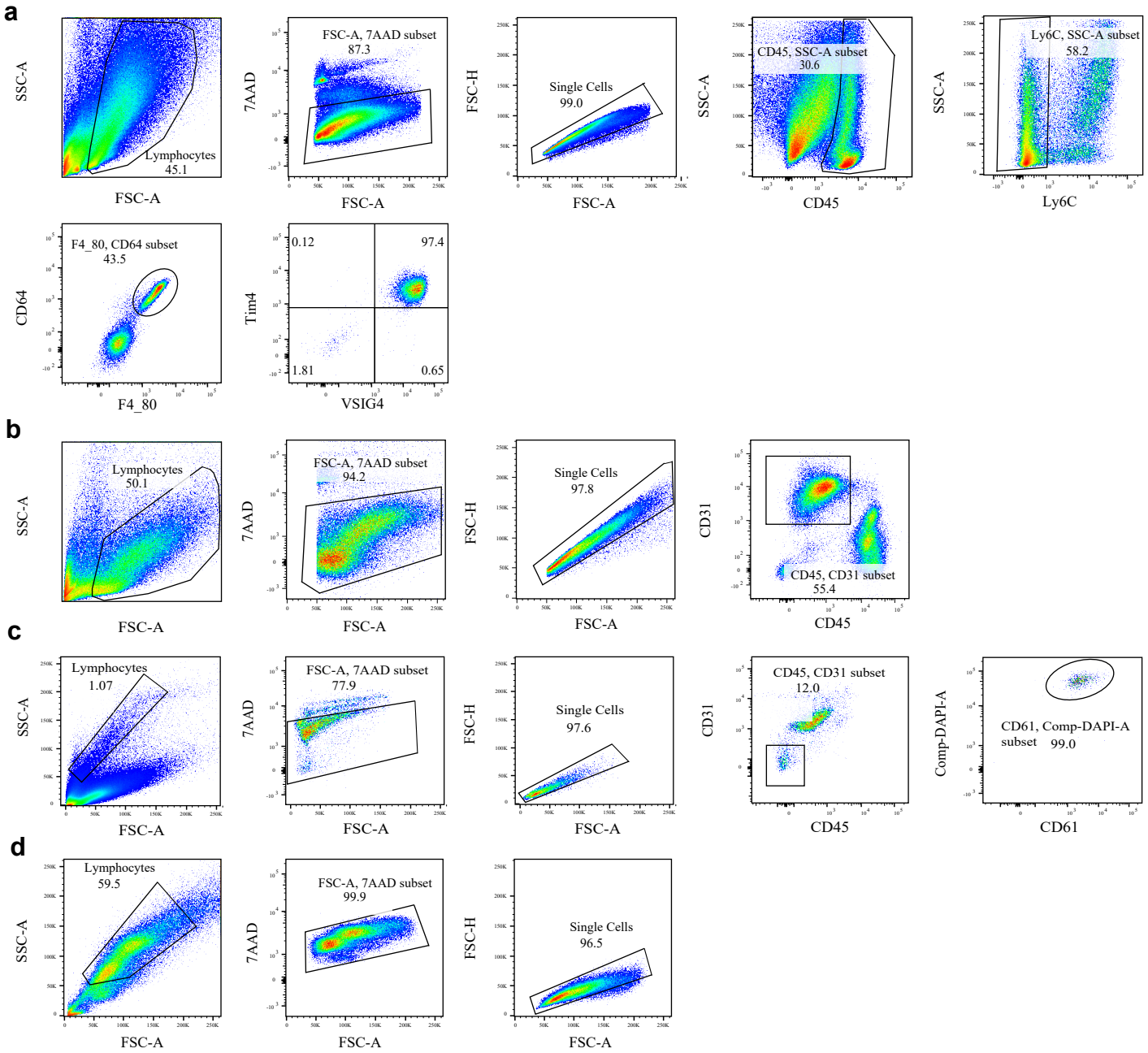

Supplementary Figure 4. Gating strategies.
(a-d) Gating strategies for KC (a), ECs (b) , HSCs (c), and HCs (d) in the liver.

Supplementary table 1. Transcription factors (TFs) downregulated in liver macrophages from BMP9/10-HSC KO mice and Smad4fl/fl Vav1-Cre mice

TFs only downregulated in liver macrophages from BMP9/10-HSC KO mice	TFs only downregulated in liver macrophages from Smad4fl/fl Vav1-Cre mice	TFs downregulated in liver macrophages from both BMP9/10-HSC KO mice and Smad4fl/fl Vav1-Cre mice
Cebpe	5730507C01Rik	Creb3l3
Creb3l2	Ahrr	Dmrt2
Epas1	Ascl2	En2
Erg	Batf3	Erf
Esrrb	Dnajc2	Hey1
Foxa3	Gm13212	Id1
Gata4	Jdp2	Id2
Gtf2ird1	Mta3	Id3
Hic1	Pax5	Irf7
Hnf4a	Pou3f1	Nr1h3
Hoxa1	Satb1	Smad7
Hoxa4	Smad4	Smad9
Hoxb5	Zfp941	Thrb
Meis2		Tlx1
Nr1i3		Zbtb18
Ppara		Zbtb4
Purg		Zfp446
Rxra		Zfp532
Six5		Zfp811
Smad6		
Spib		
Tbx3		
Tcf7l1		
Tcf7l2		
Tfec		
Tshz3		
Zfp239		
Zfp507		
Zfp951		

Supplementary Table 2. Primers used for real-time PCR.

Gene	Forward primer	Reverse primer
mouse *Pol2*	CTGGTCCTTCGAATCCGCATC	GCTCGATACCCTGCAGGGTCA
mouse *Bmp9*	CTGGAAGGAAGCATGGTCGT	CCATCCTTCGTCCCGAATGT
mouse *Bmp10*	AACGCCAAGGGGAACTACTG	TTCATACCCAGGAGGAGCGA